Self healing of creep-induced damage in Fe-3Au-4W by multiple healing agents studied by synchrotron X-ray nano-tomography

Fu, Y.; Fang, H.; Monaco, F.; Cloetens, P.; Tichelaar, F. D.; van Meel, J. G.; Brück, E.; van der Zwaag, S.; van Dijk, N. H.

DOI
10.1016/j.actamat.2022.118266

Publication date
2022

Document Version
Final published version

Published in
Acta Materialia

Acta Materialia 239 (2022) 118266

Contents lists available at ScienceDirect

Acta Materialia

journal homepage: www.elsevier.com/locate/actamat

Full length article

Self healing of creep-induced damage in Fe-3Au-4W by multiple healing agents studied by synchrotron X-ray nano-tomography

Y. Fu[a,b,*], H. Fang[c], F. Monaco[d], P. Cloetens[d], F.D. Tichelaar[e], J.G. van Meel[f], E. Brück[a], S. van der Zwaag[b,g], N.H. van Dijk[a]

[a] Department of Radiation Science and Technology, Fundamental Aspects of Materials and Energy Group, Faculty of Applied Sciences, Delft University of Technology, Mekelweg 15, Delft 2629 JB, the Netherlands
[b] Novel Aerospace Materials Group, Faculty of Aerospace Engineering, Delft University of Technology, Kluyverweg 1, Delft 2629 HS, the Netherlands
[c] CNRS SIMaP, Grenoble-INP, Université Grenoble Alpes, Grenoble 38000, France
[d] European Synchrotron Radiation Facility, Grenoble 38043 Cedex 9, France
[e] Kavli Institute of Nanoscience, National Centre for HREM, Delft University of Technology, Lorentzweg 1, Delft 2628 CJ, the Netherlands
[f] Department of Geoscience & Engineering, Faculty of Civil Engineering and Geosciences, Stevinweg 1, Delft 2628 CN, the Netherlands
[g] School of Materials Science and Engineering, Tsinghua University, Beijing 100084, China

ARTICLE INFO

Article history:
Received 16 March 2022
Revised 10 August 2022
Accepted 12 August 2022
Available online 14 August 2022

Keywords:
Self-healing
Ternary alloys
Creep damage
X-ray synchrotron radiation
Tomography

ABSTRACT

Constant stress creep experiments at 550 °C were performed on a high-purity Fe-3Au-4W (wt.%) ternary alloy with about 1 at.% supersaturation for Au and W in order to study self healing of grain-boundary cavities by both Au-rich and W-rich precipitates. Using synchrotron X-ray nano-tomography, the development of the creep cavities and the healing precipitates at different stages of creep was visualised using two spatial resolutions (30 and 100 nm voxel size) for separate samples taken after different loading times. The healing kinetics was found to strongly depend on the nucleation time of the cavities. Cavities nucleated at an early stage of creep could be fully healed, while the healing of the late-nucleated cavities is much slower due to a decrease in the diffusional flux of the healing supersaturated solutes over time, as a result of (*i*) a decrease in inter-cavity spacing caused by cavity nucleation and (*ii*) a gradual depletion of the supersaturated solutes near the grain boundaries. The interaction between the competing healing mechanisms for creep cavities by Au-rich and W-rich precipitates is discussed. It was found that Au-rich precipitates are formed much faster than the W-rich precipitates, and thereby effectively provide creep damage healing on different time scales.

1. Introduction

When exposed to a combination of a high temperature and constant stress levels even below the quasi-static yield stress, metals experience time-dependent plastic deformation, known as creep, ultimately leading to failure due to accumulated damage. Creep damage often begins with the nucleation of grain boundary cavities, which further grow and coalesce into larger cracks, which ultimately leads to failure [1]. To improve the creep resistance, the traditional mechanism is to tune the microstructure and composition of the metals such that the initiation of the cavities is postponed as long as possible [2–4]. For instance, by precipitation strengthening, solid solution strengthening, dislocation hardening, or the combination of two or more mechanisms, the dislocations and (sub) grain-boundaries can be stabilised, while grain-boundary sliding and dislocation pile-up are considered to be the reasons for creep cavity nucleation [5,6]. However, since the nucleation of the cavities has been regarded as being unavoidable, the concept of self healing [7–9] has been proposed as an alternative strategy. In self-healing metals, the early-stage cavities can be filled autonomously by the precipitation of the supersaturated solute atoms pre-dissolved in the matrix. Thereby the continuous growth and the more catastrophic coalesce of the cavities can be postponed, if not prevented. In recent years, the concept of self healing has been verified as being effective in prolonging creep lifetimes in multiple metallic systems. For austenitic stainless steels (i.e. steels having an *fcc* lattice structure at the use temperature), Laha and co-workers [10,11] reported that the combined addition of boron and nitrogen is effective in reducing the cavity growth

* Corresponding author at: Department of Radiation Science and Technology, Fundamental Aspects of Materials and Energy group, Faculty of Applied Sciences, Delft University of Technology, Mekelweg 15, Delft 2629 JB, the Netherlands.
E-mail address: Y.Fu-1@tudelft.nl (Y. Fu).

https://doi.org/10.1016/j.actamat.2022.118266

rate, as well as increasing the creep rupture strength. In a systematic study on ferritic steels (i.e. steels or alloys with a *bcc* lattice structure at the use temperature), a series experiments on binary Fe-X and ternary Fe-X-Y alloys, including Fe-Cu [12–14], Fe-Au [15–19], Fe-Mo [20], Fe-W [21] and Fe-Au-W [22], as well as simulation studies [23–25] have been conducted to reveal the healing mechanism during creep. For these model alloys the only creep damage present is the formation and growth of grain boundary cavities and the healing reaction is their autonomous filling due to the formation of solid precipitates in these cavities once formed. Several criteria are fundamental in order to achieve autonomous site-selective healing: (*i*) an extra amount of solute atoms (typically 1 at.% supersaturation at the creep temperature) need to be present in the matrix, providing the driving force for formation of precipitates; (*ii*) the nucleation energy barrier at free surfaces need to be sufficiently lower than the barrier of interior nucleation, assuring the site-selectivity; (*iii*) the solute atoms should have a higher diffusivity compared to the host atoms, so that the cavity can shrink as the vacancies diffuse outwards due to the Kirkendall effect; and (*iv*) the solute atoms should not react with other microstructural components and thereby not have been consumed before reaching the damage sites. Guided by the findings from the model alloys, a series of ferritic chrome steels with a combination of decent high-temperature mechanical properties and self-healing potential have been designed [26]. In these steels other alloying elements than the healing element, W, such as C, Cr, Ni are added to achieve decent mechanical properties, but as in the model alloys, the healing is due to only one solute atom (i.e. the healing agent).

To monitor the damage formation and the subsequent precipitation healing, multiple characterisation techniques have been applied, ranging from scanning electron microscopy (SEM) and transmission electron microscopy (TEM) to small-angle neutron scattering (SANS), where the SANS technique provides information on the nanoscale size distribution of the damage-induced precipitates. In the past two decades, synchrotron X-ray tomography has been applied as a powerful non-destructive tool to study the cavity evolution during creep [27–29]. The high-flux X-ray beam with a high collimation and monochromaticity allows fast scans with high resolution, and brings insights into early stage cavity nucleation via *in-situ* experiments [27,30]. The high coherence makes it possible to perform phase contrast imaging and holotomography [31]. Recently, Fang and co-workers [15,21] utilised synchrotron X-ray nano-tomography on the Fe-Au and Fe-W self-healing systems to monitor the development of both the creep cavities and the healing precipitates with a voxel size down to 30 nm.

In the present study, we explore the damage and healing behaviour in a Fe-3Au-4 W (wt.%) ternary system in which not one but two healing agents can act simultaneously. Au and W were selected as the most appropriate elements for such an experiment given the existence of detailed creep damage healing studies on their binary counterparts [15,21] and the difference in X-ray absorption for W and Au which may make it possible to discriminate between pore filling due to Au-rich or W-rich precipitates. In *bcc*-Fe, the solute Au and W atoms both diffuse faster than the host Fe atoms. At a temperature of 550 °C the diffusivity of Au is $D_{Au} = 7.4 \times 10^{-19}$ m^2s^{-1}, the diffusivity of W is $D_W = 3.3 \times 10^{-21}$ m^2s^{-1} and the self-diffusion of Fe is $D_{Fe} = 1.5 \times 10^{-21}$ m^2s^{-1} [25]. The higher diffusivities of Au and W are essential for an effective healing of creep cavities as it is a required condition to achieve a shrinkage of the open volume in the creep cavity by solute transport. In a previous study [23] it was discussed that the Kirkendall effect predicts a vacancy flux oriented away from the cavity when the solute has a higher diffusivity than the matrix (and towards the cavity when it is smaller). The difference in the diffusivities of the two healing agents is expected to result in a healing behaviour that operates at different time scales. Creep experiments with a constant stress of 145 MPa at 550 °C were applied and stopped after different times to investigate the microstructure development at different stages of creep. Taking the shear modulus of *bcc*-Fe at 550 °C as 65 GPa [32], the tensile stress to shear modulus ratio yields approximately 10^{-3}, while the homologous temperature T/T_m yields 0.45 (melting temperature T_m of pure iron is used). According to the creep deformation map of pure iron [33], the creep mechanism of high temperature dislocation climbing is expected to dominate. This is consistent with stress exponent $n = 4.6(5)$ from the previous research [22]. Synchrotron X-ray tomography provides a powerful tool to visualise the evolution of both the grain-boundary cavities and the precipitates within the cavities. With two voxel sizes of 100 and 30 nm, Au-rich and W-rich precipitates can be segmented. The segmentation results are compared with the SEM results from a previous research on the same ternary system [22]. The growth of cavities and the mass transfer of solute towards the damage sites are also compared with the previously studied two binary counterparts [15,21]. Considering the duration of a single creep test and the complexity of the experimental set-up, we did not perform in-situ synchrotron experiments during creep, but instead illuminated different samples exposed to the same creep condition for different times up to the lifetime of the material under the loading conditions selected. By applying high resolution X-ray synchrotron technique to the ternary Fe-Au-W model alloy with two healing solutes, we investigate the evolution of damage cavities and the healing precipitates at different stage of creep, and the interaction between the two healing agents.

2. Experimental

2.1. Sample preparation and creep tests

High-purity Fe-Au-W alloy sheets were ordered from GoodFellow. The composition of the samples is Fe-3.8W-3.1Au (in wt.%). Dog-bone shaped creep samples with a gauge length of 12.5 mm and a cross-section of 3 mm^2 (6 mm width and 0.5 mm thickness) were cut by spark erosion. The samples were then sealed in quartz tubes filled with 200 mbar ultra-high purity argon to prevent oxidation during annealing. After the homogenising process (at 868 °C for 5 h), the samples were quenched in water. The as-quenched samples were examined with scanning electron microscopy to assure a uniform homogenised matrix in which no precipitates can be observed before creep tests. The solutionised as-quenched samples showed an average grain size of 77 μm. A limited amount of $FeWO_4$ particles could be detected in the grain interior both for the as-received and creep-loaded samples. These particles are expected to remain stable during creep and they do not show an obvious effect on the grain boundary cavity formation or the healing. The microstructure of the as-quenched sample is shown in Fig. S1 (supplementary information).

The creep experiments were performed in vacuum at a fixed temperature of 550 °C with a constant stress of 145 MPa. The creep lifetime is estimated to be inversely proportional to the steady strain rate, which fulfils the Sherby-Dorn equation [34]$\dot{\varepsilon}_S = Ad^m\sigma^n\exp(-Q/RT)$, where A, where A is a structure dependent constant, d is the grain size, m is the grain size exponent, σ is the applied stress, n is the stress exponent, Q is the activation energy, R is the gas constant and T is the temperature in kelvin. Taking the stress exponent $n = 4.6$ [22] and assuming the grain size exponent m the same as that of the Fe-Au alloy ($m = -2$ [18]), the estimated lifetime of the ternary Fe-Au-W alloy with the grain size of 77 μm yields 240 h. In order to study the microstructure development at different stages of creep, the creep experiments were interrupted after 10, 50, 100, 150 and 223 h. The microstructure in the uniform deformation region was characterised

via scanning electron microscopy (SEM) using a JEOL JSM 6500F instrument equipped with energy-disperse X-ray spectroscopy (EDS). To reveal the precipitate crystal structure and composition, transmission electron microscopy (TEM) measurements were performed using a FEI C_s-corrected cubed Titan instrument. Elemental analysis was done with the Thermo Fisher Scientific super-X detector in the ChemiSTEM^{TM} configuration. Lattice images were collected on a Gatan camera. ADF (Annular Dark Field) images and EDX spectra for elemental mapping were collected in STEM (Scanning Transmission Electron Microscopy) mode.

2.2. Synchrotron X-ray nano-tomography

The interrupted creep samples were further machined for the tomography experiments. Rectangular samples with a cross section of 300 × 300 μm^2 and a length of approximately 6 mm were cut from the uniform deformation region by spark erosion, with their long axis aligned with the loading direction during creep. Tomography measurements were performed at the ID16A-NI nano-imaging beamline of the European Synchrotron Radiation Facility (ESRF) in Grenoble, France [35]. The beamline provides a high-brilliance beam focused down to nano size (13 nm), allowing the observation of 3D microstructure for the creep-induced cavities and the precipitates formed in the cavities. The rectangular samples were mounted on a rotation stage and illuminated by the X-ray beam. A series of 2D X-ray projections (in total 1800 projections for each scan) were recorded as the sample rotated around an axis over 180° at 4 focus-to-sample distances for the phase retrieval [31]. Combining the information at the 4 distances, the phase map for each angle was obtained running inhouse developed GNU Octave scripts. With the ESRF PyHST software package [36], the obtained phase maps were reconstructed to 3D digital images. For each sample, two resolutions were used with the corresponding voxel sizes of 100 and 30 nm. The volume of view (VoV) of the 30 nm scan is selected within the VOV of the 100 nm scan, allowing one to compare the microstructure of a same region with different resolutions. The 100 nm and 30 nm scans yield reconstructed volumes of 321.6 × 321.6 × 321.6 μm^3 and 96.48 × 96.48 × 96.48 μm^3, respectively. The VoVs to be analysed were selected by on-line prior inspection of the X-ray images. The VoV should contain at least one grain boundary perpendicular to the loading direction, to show some form of creep damage and to be fully contained in the sample, preferably as close to the central axis as possible.

2.3. Phase segmentation and quantitative analysis

The subsequent tomographic rendering and phase segmentation are performed with the FEI Avizo software. From the microstructure characterisation and in line with previous electron microscopy studies [22], 4 phases are detected in the creep-failed Fe-Au-W samples, namely the *bcc* matrix, the *fcc* Au-rich precipitates (with an Au concentration of about 60 at.%), the W-rich precipitates with the composition of Fe_2W, and the cavities. The occasional $FeWO_4$ particles are not taken into consideration since they do not affect the damage formation and self-healing behaviour. The electron densities of the precipitates can be estimated based on their composition and crystal structure. Since the electron densities of the precipitates (3.71 e/Å^3 for $Au_{60}Fe_{40}$ and 3.38 e/Å^3 for Fe_2W, respectively) are higher than that of the matrix (2.21 e/Å^3 for Fe) and even more so for the cavities (vacuum), the precipitates (including the Au-rich and W-rich ones) and the cavities can be separated from the matrix by applying carefully selected threshold values to the grey value in the reconstructed slices. In the current work, the features with a higher electron density have a lower grey scale value, while a lower electron density results in a higher grey scale value. This means that in the reconstructed slices the precipitates are darker than the matrix, while the cavities are brighter.

In addition to the thresholds $I_{ppt/m}$ and $I_{cav/m}$ to separate the precipitates, cavities and the matrix ($I_{ppt/m}$ is the threshold between the precipitates and the matrix and $I_{cav/m}$ the threshold between the cavity and the matrix), another threshold $I_{Au/W}$ ($I_{Au/W} < I_{ppt/m}$) is required to further segment the Au-rich and W-rich precipitates. Based on the microstructures of the precipitates (further discussed in Section 3.2) and previous results [22], the two types of precipitates are found to form separately for most of the cases. Therefore, it is safe to label a precipitate either Au-rich or W-rich. For each labelled precipitate, if the majority of its voxels have a grey scale between $I_{Au/W}$ and $I_{ppt/m}$, this precipitate is categorised as W-rich. Due to the small size of the W-rich precipitates, the segmentation of the Au-rich/W-rich precipitates is only applied to the scans with a voxel size of 30 nm (and not for the scans with a voxel size of 100 nm). For both resolutions, objects (precipitates and/or cavities) with a volume smaller than 8 voxels (i.e. with a volume smaller than 8 × 10^{-3} and 2.16 × 10^{-4} μm^3 for the scans with a voxel size of 100 nm and 30 nm, respectively) were regarded as noise, and therefore ignored.

After the phase identification, the binary images were used for further analysis in MATLAB using the DIPimage toolbox [37]. For each object (cavity or precipitate), its shape was determined by the shape complexity, its elongation and flatness [15,21]. The elongation and flatness are calculated from the three semi-axes of an equivalent ellipsoid with the same moments of inertia as the object itself. It is assumed that the volume occupied by a precipitate was previously occupied by an open cavity. By checking the contact between the precipitates and the open volume for each cavity, we determine how many precipitates are contributing to fill the cavity, how much volume has been filled, and how much volume remains open. The total volume of a cavity is therefore $V_{cav} + V_{prec}$, where V_{prec} is the volume of the precipitates in contact with the open volume V_{cav}. The filling ratio of an individual cavity is therefore $FR = V_{prec}/(V_{cav} + V_{prec})$. More detailed on the applied methodology for the shape classification and the filling ratio calculation can be found in reference [15]. A quantitative analysis is applied based on the scans with a 100 nm resolution, which provide a larger illuminated volume and therefore a better statistical significance. A volume rendering for the same region of interest (ROI) with both the 100 nm and 30 nm voxel sizes is shown in Fig. S2 (supplementary Information). As expected, the two resolutions provide similar results for objects with a relatively large size, while some difference can be observed for the smaller objects and more detailed features can be distinguished for the smallest voxel size.

3. Results

3.1. Creep results

The strain-time curves of the creep experiments at a stress of 145 MPa and a temperature of 550 °C are shown Fig. 1. The steady-state creep begins with a relatively constant strain rate soon after the load is fully applied. Given the reproducibility of these creep curves interrupted at different times, the general characteristics of the creep-induced cavities and the corresponding healing precipitates can be monitored as a function of time. It is clear that the samples interrupted at 10, 50, and 100 h are in the steady-state creep regime, while the two samples with longer times (150 and 223 h, respectively) show an onset towards tertiary creep, where the strain rate increases rapidly compared to the steady-state creep, as indicated by the dashed arrows. It is found that the strain contribution from the steady-state creep is less than 1%, which is consistent with previous results on the same alloy [22]. The strain rate for the 5 samples lies between

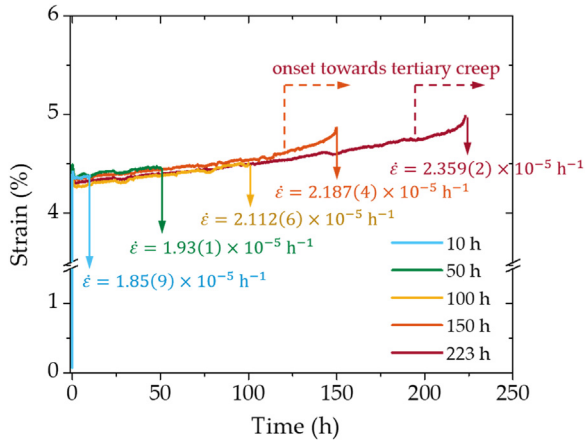

Fig. 1. Creep curves for the Fe-Au-W alloy samples with a constant applied stress of 145 MPa at a temperature of 550 °C. The creep experiments were interrupted after the indicated creep times.

1.85(9) × 10^{-5} h^{-1} and 2.359(2) × 10^{-5} h^{-1}, with an average strain rate of 2.09(4) × 10^{-5} h^{-1}. As stated in the introduction, the combination of the stress level and the operating temperature is expected to result in a power-law creep, more specifically, the creep is dominated by high temperature dislocation climbing. The above derived strain rates agrees well with the mechanism [33]. Taking the steady-state creep rate for the ternary alloy with different grain sizes (77 μm in the present study and 103 μm in the previous study [22]), a grain size exponent of $m = -2.2$ is deduced. This grain size exponent indicates that the creep is controlled by both dislocation climbing and diffusion [38].

3.2. Microstructure of the creep samples

Fig. 2(a) shows a SEM image of a grain boundary with grain-boundary cavities and healing precipitates for the Fe-Au-W alloy sample with a creep time of 223 h (at 145 MPa and 550 °C). Several grain-boundary cavities are fully filled by relatively large precipitates (indicated by yellow arrows), while others show a very limited degree of filling, and only nano-sized precipitates can be observed inside the cavities (indicated by blue arrows). EDS results demonstrate that the larger precipitates in the cavities with a high filling ratio are significantly enriched in Au (about 18 at.% Au), while the nano-sized precipitates in the cavities with a limited filling ratio are generally enriched in W (1.8–4.8 at.% W). Apart from the precipitates formed exclusively at the free surface of the cavities, nano-sized Au-rich precipitates can also be observed in the matrix, as indicated by the triangular region. As shown in Fig. 2(b), these precipitates are found to be disc-shaped and are generally connected with dislocations formed during creep. These disk-shaped Au-rich precipitates are restrained from growing, due to the strain energy resulting from the mismatch between the precipitate lattice and the matrix lattice [18]. Examples for dislocations and the strain contrast are indicated by the red arrows and circles in Fig. 2(b). It is worth to note that the disc-shaped Au-rich precipitates can be consumed by the nucleation and growth of the healing precipitates in the nearby cavities [18]. In fact, on the upper side of the grain boundary in Fig. 2(a), a depletion zone is formed, where fewer Au-rich nano-sized precipitates can be observed. It is deduced that during the creep, the disc-shaped precipitates in the depletion zone are dissolved into the matrix and diffused towards the grain boundary in the form of Au atoms, through which they are further transported to the cavities and nucleate as Au-rich healing precipitates [18].

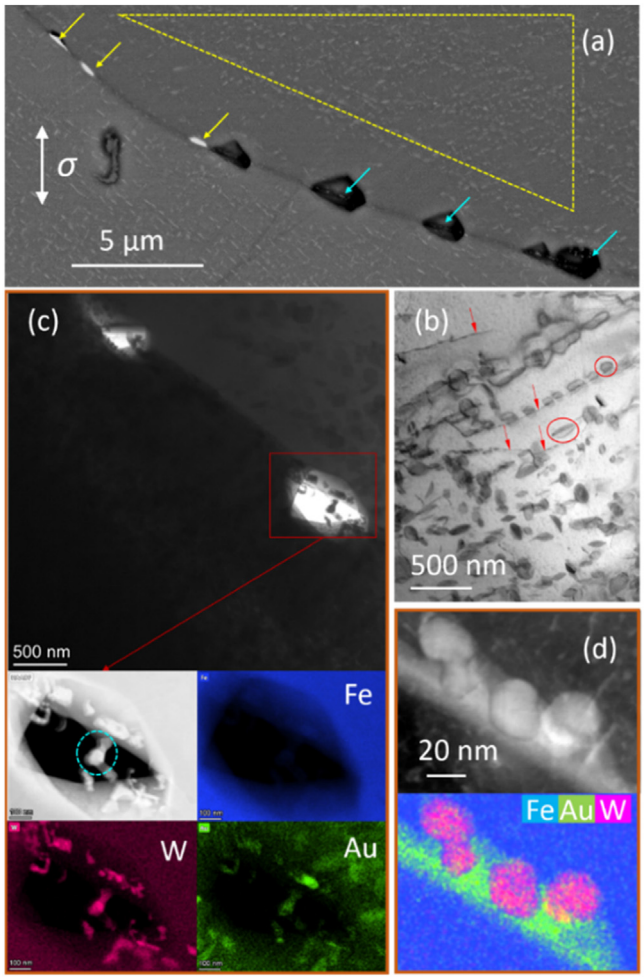

Fig. 2. SEM and TEM data for the Fe-Au-W alloy sample after 223 h creep with a constant applied stress of 145 MPa at 550 °C. (a) SEM image of a grain boundary and its vicinity. The yellow arrows indicate cavities that are filled by Au-rich precipitates, while the blue arrows indicate the nano-sized W-rich precipitates that show a limited degree of filling. Nano-sized Au-rich precipitates in the matrix are indicated by the dashed triangle. In between of the grain boundary and the triangular region with nano-sized Au-rich matrix precipitates, a precipitate-free depletion zone is observed. (b) TEM bright field (BF) image for the nano-sized Au-rich precipitates. The red arrows and circles indicate the dislocations and strain contrast, respectively. (c) TEM BF and high angle annular dark field (HAADF) images with EDX maps for grain-boundary cavities. The encircled precipitate is mainly enriched in W (29 at.%) while its Au concentration is slightly higher (4 at.%) than nominal. (d) Example for co-existence of the Au-rich and W-rich precipitates at a grain boundary. The Au-rich and W-rich precipitates have formed in contact to each other, rather than in the form of isolated precipitates (For interpretation of the references to color in this figure legend, the reader is referred to the web version of this article.).

The TEM bright field (BF) and high angle annular dark field (HAADF) images with the EDX maps reveal the morphology and the composition of the nano-sized precipitates in the partially-filled cavities, as shown in Fig. 2(c). Consistent with the SEM-EDS result, most of the precipitates located at the cavity surface with a low filling ratio are enriched in W; for example, the precipitate indicated by the dashed blue circle has 29 at.% W and 4 at.% Au. The composition of the precipitates is in line with the expected composition of the Fe_2W Laves phase. Due to the limited size of the W-rich precipitates, it was difficult to uniquely establish the lattice structure. Previous creep studies on the same ternary Fe-Au-W alloy [22] and on the related binary Fe-W alloy [21] did confirm the presence of the Laves phase by HREM. In a surface precipitation study on the same ternary Fe-Au-W alloy, where the precipitation

on the external free surface was aimed to mimic the precipitation on internal creep-induced grain-boundary cavities [39], the Laves phase was also detected by EBSD after 32 h annealing. In the remainder of the text these precipitates are referred to as 'W-rich precipitates'. The co-existence of Au-rich and W-rich precipitates is found both at cavity surfaces (e.g. Fig. 2(c)) and at grain boundaries. An example of this co-existence is given in Fig. 2(d): the Au-rich and W-rich precipitates form in contact to each other, instead of forming isolated. The Au-rich precipitates were confirmed to show an *fcc* structure with a composition of about 60 at.% Au.

3.3. Tomographic rendering

Fig. 3 shows a 3D overview of the creep cavity and healing precipitate distribution in the samples with creep times ranging from 10 to 223 h for a voxel size of 100 nm. The TEM results in Fig. 2 indicate that the W-rich precipitates generally have a size of about 100 nm (consistent with previous results [22]), which is comparable to the resolution of this scan. Therefore, all the precipitates will be combined in the analysis of the 100 nm resolution data, without classification in either Au-rich or W-rich precipitates. The cavities and precipitates are represented by orange and blue volumes, respectively. It is clear that with the increase in creep time: (1) more features can be observed and (2) the features, including the cavities and the precipitates, are growing in size. In the sample after 10 h of creep, some cavities and sporadic precipitates are observed, with an average equivalent diameter of 0.54 μm for the cavities and 0.41 μm for the precipitates. Most of the cavities are empty, indicating that the cavities are in their initial growth state just after nucleation. In the sample after 50 h of creep, more features (especially more precipitates) are observed in comparison to the sample after 10 h of creep. In addition, the cavities and precipitates start to show interaction: one or more precipitates are usually found in the vicinity of a cavity, indicating that the precipitates have multiple nucleation sites at the cavity surface. From 50 to 100 h of creep, both the cavities and the precipitates experienced obvious growth. Most of the cavities and the precipitates are located at the grain boundaries, especially at the transverse grain boundaries oriented perpendicular to the load direction. Cavities on some grain boundaries are significantly elongated, indicating a fast propagation of the cavities. In the binary Fe-Au [15] and Fe-W [21] samples, a significant amount of cavities were found to show a linkage of neighbouring cavities in the later stages of creep, in some cases resulting in cavities covering the whole grain boundary with the volume larger than 1000 μm^3. The cavity linkage is also observed in the current ternary Fe-Au-W system for the longest creep times (150 and 223 h). However, due to the limited creep strain in the ternary system, the linkage phenomenon is not as obvious as in the binary counterparts. The largest open volume found in the 223 h sample was less than 200 μm^3.

Figs. 4 and 5 show examples of the cavities and precipitates from samples with different creep times. As illustrated in Fig. 4, in the sample after 10 h of creep most of the cavities have an elliptical or spherical shape: three cavities with a size of about 1 μm are aligned along the grain boundary direction. After 50 h of creep, the average equivalent diameter of the cavities increased from 0.54 μm (10 h) to 0.74 μm (50 h), and one or more precipitates are found to nucleate at the surface of the cavities. It is also worth to note that for the cavities, more complex shapes have developed, even though the increase in size is limited compared to the sample with 10 h of creep. Where the cavities after 10 h of creep usually have an ellipsoidal shape with smooth surfaces, after 50 h the cavities show more detailed features with tails and edges. As indicated by the black arrows (Fig. 4(b), top view), the cavities appear to grow only in specific directions (as indicated by the white arrows), as for other directions the growth is restricted by precipitation. This anisotropic growth results in cavities with more complex shapes compared to the ones observed in the 10 h sample (which had limited to time to grow after nucleation). The competition between cavity growth and precipitate healing is more obvious in the first example for the sample after 150 h of creep (Fig. 5(a)): the precipitates form around the cavity surface until the cavity is eventually wrapped by the precipitates. For the longer creep times a linkage of cavities is observed for part of the cavities. Fig. 5(b) provides a clear example showing the early stage of linkage between two neighbouring cavities (indicated by the yellow boxes). A late stage of linkage can be observed in Fig. 5(c,d), where the linkage of cavities results in a cleavage of the grain boundaries. In Fig. 5(b), the precipitates are observed at the notch of the cavity (indicated by the solid black circles) and the linking point between the two cavities (indicated by the dashed black circles). The morphology of the cavities and precipitates provides indirect evidence that the precipitates are formed after the occurrence of the cavities.

In Fig. 6, an example of the further segmentation of Au-rich and W-rich precipitates at the enhanced resolution of 30 nm for the sample with the longest creep time of 223 h. Fig. 6(a,c) show a region of interest (ROI) with a volume of $30 \times 30 \times 40$ μm^3 from different directions. The red, yellow and blue volumes represent the cavities, the Au-rich precipitates and the W-rich precipitates, respectively. It is clear that about half of the cavities are fully filled by Au-rich precipitates, while the other cavities show very limited degree of filling. Small W-rich precipitates are frequently found in the partly filled cavities, showing a limited filling capacity due to its low diffusivity. The green dashed box in Fig. 6(c) shows cavities that are fully filled with Au-rich precipitates, and even shows a clear linkage of neighbouring cavities. Fig. 6(d,e) show two cavities partly filled by both Au-rich and W-rich precipitates. On the left, the precipitates and cavities are shown separately, while on the right, a larger transparent red contour is presented to indicate the original cavity with no healing for better visualisation. The contour is generated by dilating the sum of all the three phases (cavity, Au-rich precipitate and W-rich precipitate) by two voxels.

These observations are consistent with the previous SEM results at the fracture surface of creep failed samples of the same Fe-Au-W alloy [22]. Fig. S3(a) (Supplementary Information) shows details of features on a grain boundary located at the fracture surface after creep. The white precipitates (4 examples are indicated by yellow arrows) are mainly enriched in Au, and the corresponding cavities are fully filled by these Au-rich precipitates. Meanwhile, other cavities are still open (4 examples are indicated by red arrows), and only small precipitates with equivalent diameters of about 100 nm are observed at the surface of the open cavities. Most of the nano-sized precipitates are found to be enriched in W, as indicated by blue arrows in Fig. S3(c,d). Examples of cavities that are fully filled by Au-rich precipitates with linkage between neighbouring cavities as observed in Fig. 6(c) can also be observed in the SEM image at the fracture surface of the creep failed sample, as indicated by green boxes in Fig. S3(b). The examples shown in Fig. S3(b,d) indicated by the dashed red curves show two cavities partly filled by both Au-rich (yellow arrows) and W-rich (blue arrows) precipitates similar to the examples of Fig. 6(d,e).

3.4. Shape and linkage of cavities

In previous studies on the creep damage healing of cavities in the two binary counter systems [15,21], the cavities were categorised into either isolated or linked cavities. The majority of the cavities was found to correspond to isolated ones. The number density of linked cavities was one order of magnitude lower than that for the isolated cavities. However, although the linked cavities were less frequently observed, they contributed more to the volume fraction, as they were generally much larger in size.

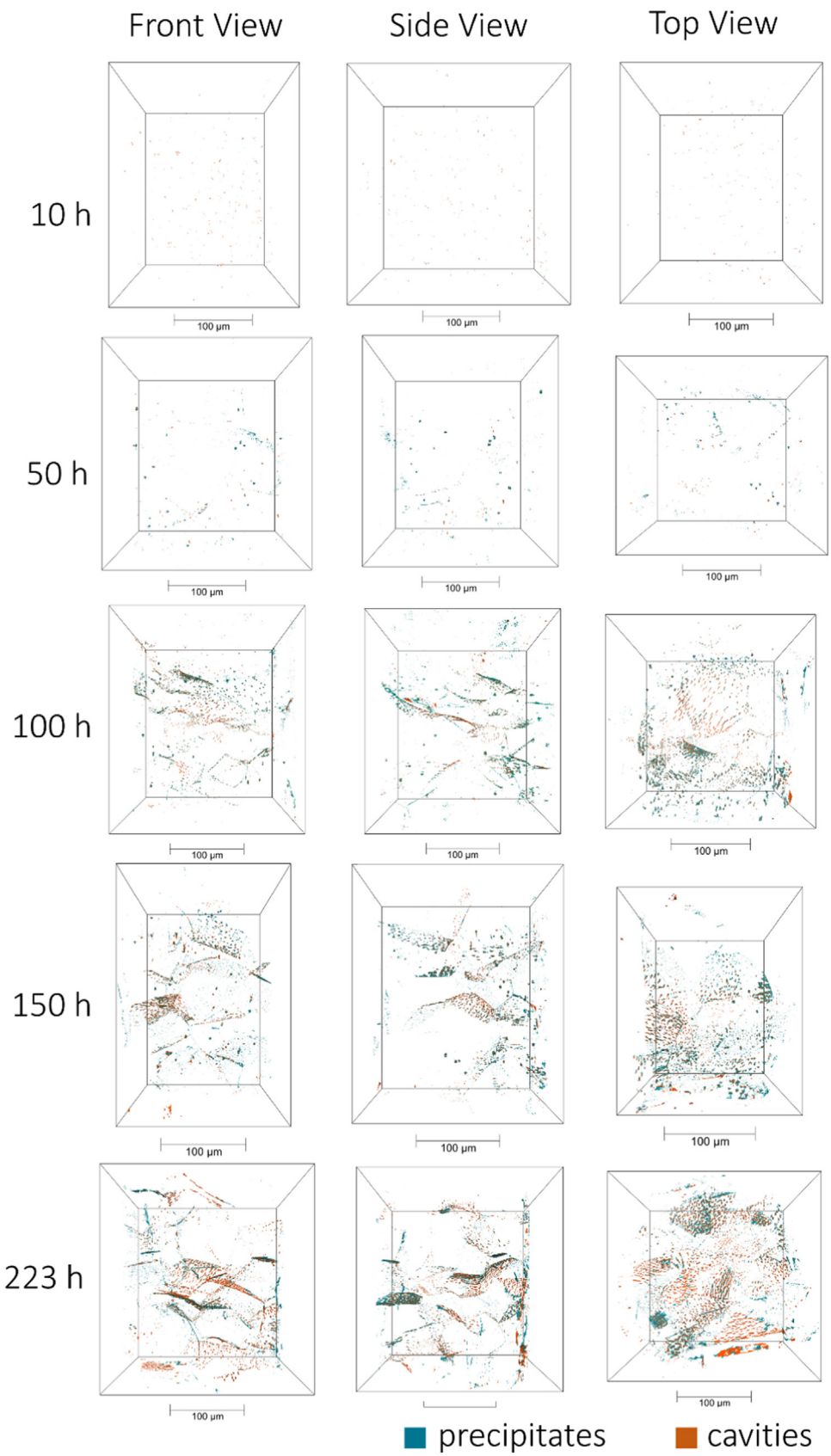

Fig. 3. Segmented volume rendering showing the distribution of cavities (orange) and precipitates (blue) in the Fe-Au-W alloy after creep at 550 °C with a constant applied stress of 145 MPa for different times. The images are obtained with a voxel size of 100 nm. The applied stress is normal to the top view (For interpretation of the references to color in this figure legend, the reader is referred to the web version of this article.).

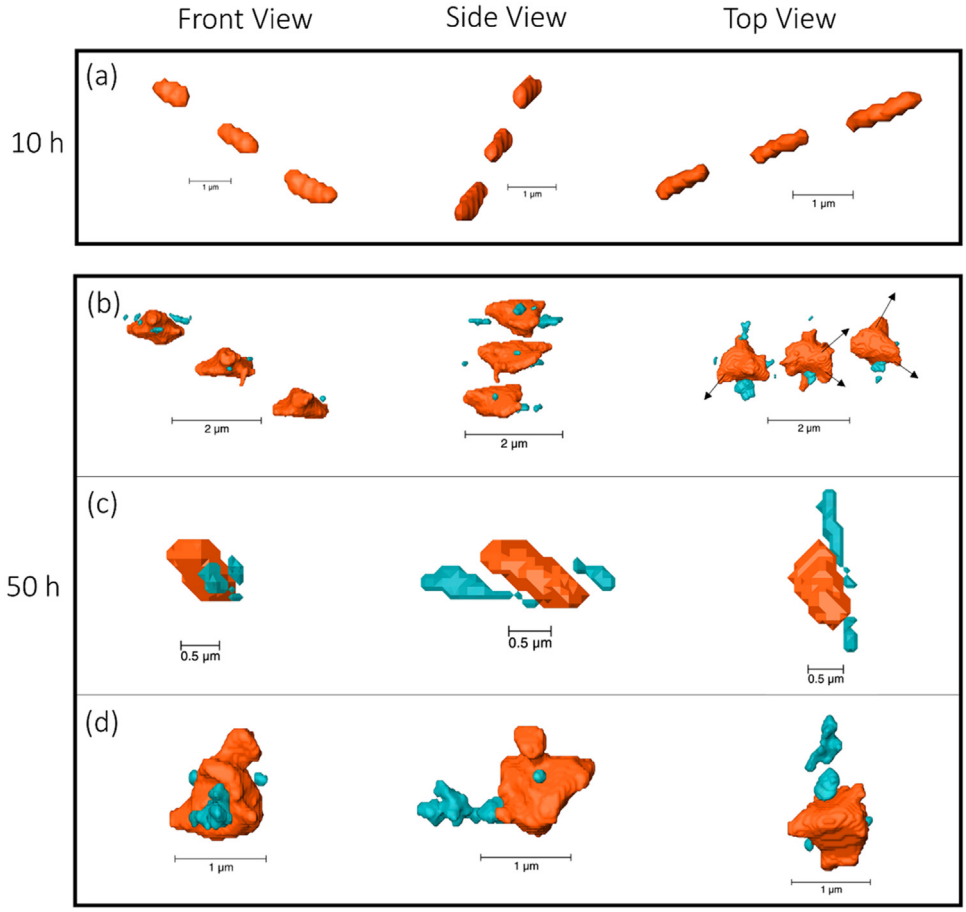

Fig. 4. Examples of segmented volume rendering for early-stage creep cavities and healing precipitates after (a) 10 h and (b)–(d) 50 h creep. The orange and blue volumes indicates cavities and precipitates, respectively. The black arrows in (b) indicate the growth direction of the cavities (the cavity growth in other directions seem to be blocked by the precipitates) (For interpretation of the references to color in this figure legend, the reader is referred to the web version of this article.).

In the present work, we use the shape classification and the linkage criteria introduced in references [15,21]. Based on their elongation, flatness and complexity values the cavities are grouped into: (*i*) sphere, (*ii*) equiaxed, (*iii*) rod, (*iv*) sheet and (*v*) complex. The sphere and equiaxed shaped cavities are expected to be isolated, while the rod, sheet and complex shaped cavities are further identified as linked if their major axis exceeds the average inter-cavity spacing.

In Fig. S4 the number density and volume fraction for different shapes and types (isolated or linked) are shown as a function of the creep time. Unlike the results for the binary Fe-Au and Fe-W systems [15,21], the linked cavities in the ternary Fe-Au-W system do not contribute significantly to the number density and volume fraction. Due to the limited strain in the creep experiments of the Fe-Au-W system, it is not likely that the isolated cavities link with multiple neighbours and develop into large-scale cavities. In the ternary system, the linked cavities are generally only twice as large as the isolated cavities. The average equivalent cavity diameter after a creep time of 100 h, 150 h and 223 h corresponds to 0.92(1), 1.09(1) and 1.17(1) μm for the isolated cavities and 1.89(7), 1.93(6) and 2.09(6) μm for the linked cavities, respectively. Therefore, unless specified otherwise, in the present study we treat all the cavities and precipitates together without categorising them in isolated or linked cavities.

3.5. Filling ratio

To quantify the creep damage as well as the degree of healing it is crucial to measure both the (remaining) cavity volume as well as the precipitate volume formed inside that cavity. For an individual cavity, the ratio between the precipitate volume formed inside the cavity and the sum of the precipitate volume and the open volume of the cavity is defined as the filling ratio *FR*. For an empty cavity $FR = 0$ and for a fully filled cavity $FR = 1$. In Fig. 7 the filling ratio of each cavity is plotted as a function of its cavity volume (precipitates and open volume) at different creep times. With increasing creep time the volume of the unfilled, partly-filled and fully-filled cavities spans over a wider range of volumes, indicating a continuous cavity growth and a continuous precipitate healing. The lower limit of the unfilled cavities is determined by the resolution of the tomography, which indicates that cavity nucleation keeps taking place during the whole creep process. The upper limit of the unfilled cavities increases with time, indicating that some of the cavities remain unfilled through the creep process without any sign of precipitation (within the resolution limit). The maximum volume of the fully healed cavity also increases with time, which again indicates that the healing takes place continuously and that larger cavities can start to become filled after a longer time of existence. In the binary Fe-W system [15,21], the maximum volume of the unfilled cavities is orders of magnitude larger than the fully-filled ones. In the current ternary Fe-Au-W system, however the maximum volume of the unfilled and fully filled cavities are comparable for a fixed creep time. This difference may originate from the limited cavity linkage in the ternary system (as shown in Fig. 3 and described in Sections 3.3–3.4).

For a creep time of 10 h, the filling ratio is generally either 0 or 1 (see Fig. 7(a)), since the cavities and precipitates are small and partial filling can not be detected reliably, and few interactions be-

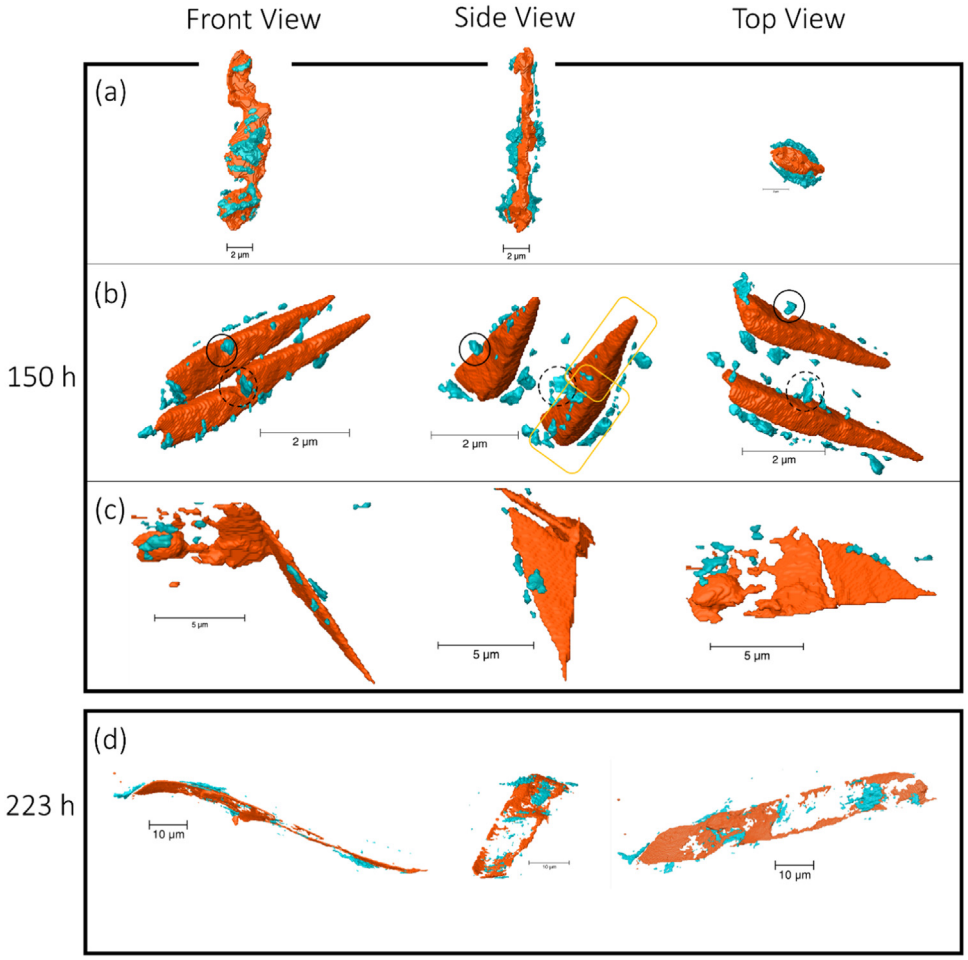

Fig. 5. Examples of segmented volume rendering for late-stage creep cavities and healing precipitates after (a) – (c) 150 h and (d) 223 h creep. The orange and blue volumes indicates cavities and precipitates, respectively. Yellow boxes indicate the linkage of two originally isolated cavities. Precipitates were found at the notch and at the linking point of the cavities, as indicated by the solid and dashed circles, respectively (For interpretation of the references to color in this figure legend, the reader is referred to the web version of this article.).

tween them are observed (see Fig. 3(a)). For a creep time of 50 h precipitates are found to nucleate at the surface of the cavities (see Fig. 3(b)), resulting in a filling ratio ranging from 0 to 1 (Fig. 7(b)). For a longer creep time (Fig. 7(c–e)), the filling ratio continues to cover the whole range from 0 to 1. The observed distribution of filling ratios results from the continuous nucleation and growth of the cavities and the continuous filling of the open volume by the precipitates. In Fig. 7(f), the average filling ratio $<FR>$ as a function of the average cavity size $\langle V \rangle$ is presented for the partly-filled cavities. With an increase in creep time, the average cavity volume increases while the average filling ratio decreases. This indicates that for longer creep times the cavity filling progressively lags behind the cavity growth (especially for the large ones).

4. Discussion

4.1. Time evolution of the cavities and precipitates

To monitor the time evolution of the cavities and the precipitates during creep, we have categorised the cavities into three groups: (*i*) empty, (*ii*) partially-filled and (*iii*) fully-filled. The number density and volume fraction as a function of creep time are summarised in Fig. 8 for these three categories. Several results can be observed from Fig. 8: (1) For the empty cavities both the number density and volume fraction show an increase with creep time, confirming a continuous cavity nucleation (as described in Section 3.5). (2) For the fully-filled cavities an obvious increase in both the number density and volume fraction with creep time is observed during the whole creep process. This is in line with the results in Fig. 7 and proves that the healing of the cavities takes place continuously. (3) For the partially-filled cavities both the number density and the volume fraction initially show an increase before they stabilise at a roughly constant level after 100 h. A stabilisation of the number of partially filled creep cavities is expected for a continuous process of concurrent creep cavity nucleation, cavity growth and cavity filling. When the cavity nucleation rate, cavity growth rate and the cavity filling rates are more or less stable in time then the number density of partially filled cavities will also stabilise as after an initial stage the rate at which new cavities are formed and existing cavities are fully filled will equalise in a steady-state creep process. It is worth to note that the number density of the precipitates in the partially-filled cavities is higher than that of the corresponding cavities. This indicates that multiple precipitates are formed in a single cavity during the healing process (on average about 3 to 4 precipitates per cavity). This is in agreement with the examples shown in Figs. 5 and 6. (4) The partially-filled cavities and the precipitates therein both experience an increase in volume fraction, but the volume fraction of cavities increases faster, resulting in a decrease in the filling ratio (as illustrated in Fig. 7(f)).

Fig. 9 summarises the distribution in orientation of the cavities and the precipitates as a function of the angle between the

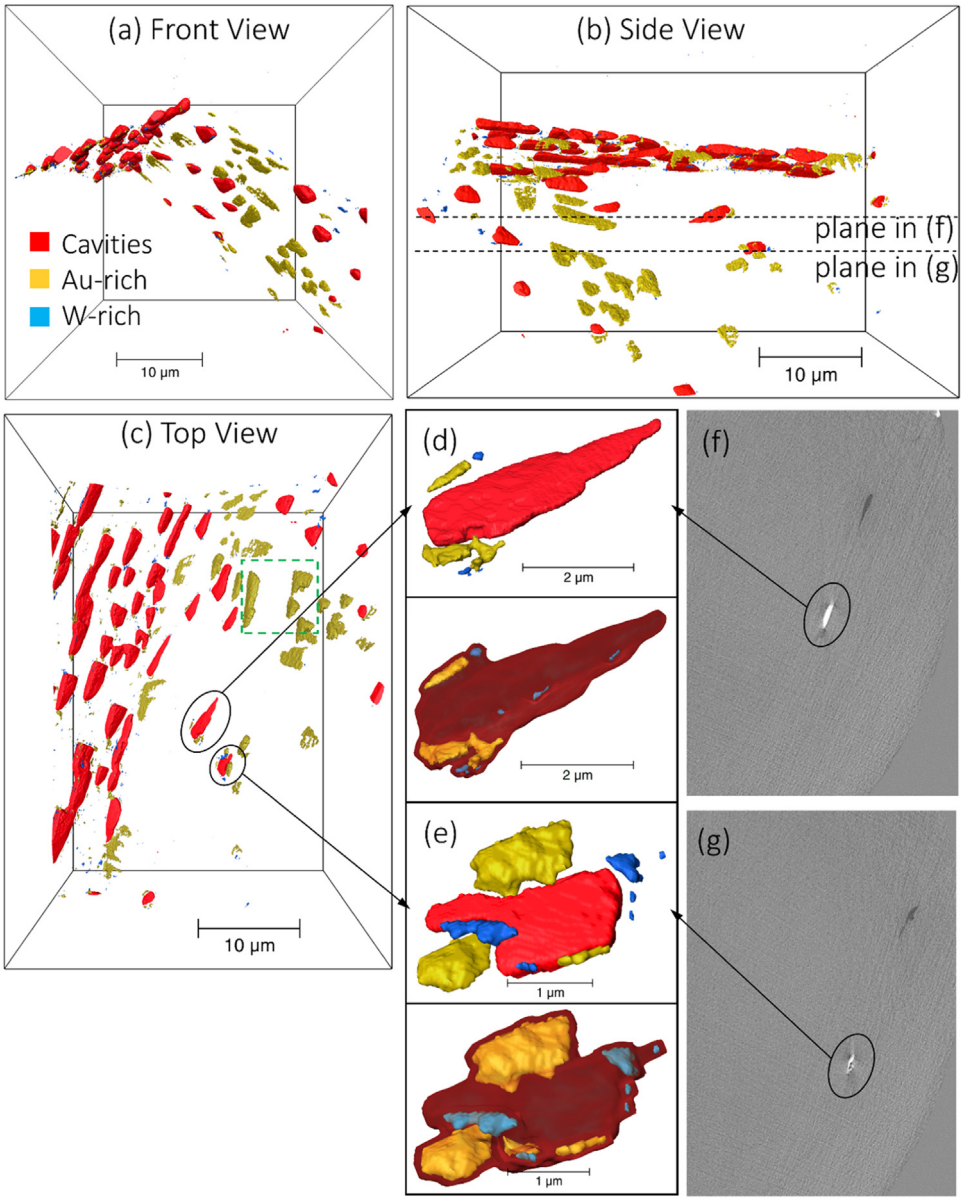

Fig. 6. Example of the further segmentation of Au-rich and W-rich precipitates in the 223 h sample. (a)–(c) Front view, side view and top view for a region of interest (ROI) with a volume of 30 × 30 × 40 μm^3. (d,e) Two examples of cavities partly filled by both Au-rich and W-rich precipitates. The precipitates and open volumes are shown separately at the top, while for better visualisation, larger transparent contours are presented at the bottom to indicate the original cavity in the absence of healing. (f,g) Two tomography slices normal to the stress direction. The circles in (f,g) correspond to the partially-filled cavities in (d,e), respectively. The green box in (c) shows examples of fully filled cavities, some after linkage with their neighbours. The dashed lines in (b) indicate the position of the slices in (f,g) (For interpretation of the references to color in this figure legend, the reader is referred to the web version of this article.).

long axis of the cavity/precipitate and the stress direction. For the shortest creep time (10 h) the freshly nucleated cavities show no preferred orientation. With an increase in creep time to 50 h and beyond, most cavities are found to form with an angle close to 90°, indicating that the creep cavities prefer to nucleate at the grain boundaries oriented perpendicular to the stress direction (load-bearing grain boundaries) and that they tend to propagate in the grain boundary surface. The precipitates also show a preference for a 90° angle with respect to the loading direction for a creep time of 100 h and beyond. The time lag in the formation of the preferred orientation for the precipitates (at $t \approx 100$ h) after the preferred orientation is observed for the cavities (at $t \approx 50$ h) provides strong evidence that the creep cavities initiate the formation of precipitates. Cavity nucleation has already started at the earliest creep time of 10 h, while the preferred orientation of the cavities only develops between 10 and 50 h. The precipitates nucleate after the occurrence of the cavities, and they subsequently grow in accordance with the shape of the cavities. This behaviour is consistent with the results from the previous study on the binary Fe-Au system [18].

To compare the cavity and precipitates sizes in the ternary Fe-Au-W alloy with the two binary Fe-Au and Fe-W counterparts, the number distribution of the cavities and the precipitates are fitted to a log-normal distribution:

$$D_N(d) = \frac{N_0}{d\omega\sqrt{2\pi}} \exp\left(-\frac{\left(\ln d - \ln \bar{d}\right)^2}{2\omega^2}\right) \quad (1)$$

where N_0 is the number density, d the equivalent diameter, $\bar{d}$ the mean equivalent diameter and ω the relative width of the distribu-

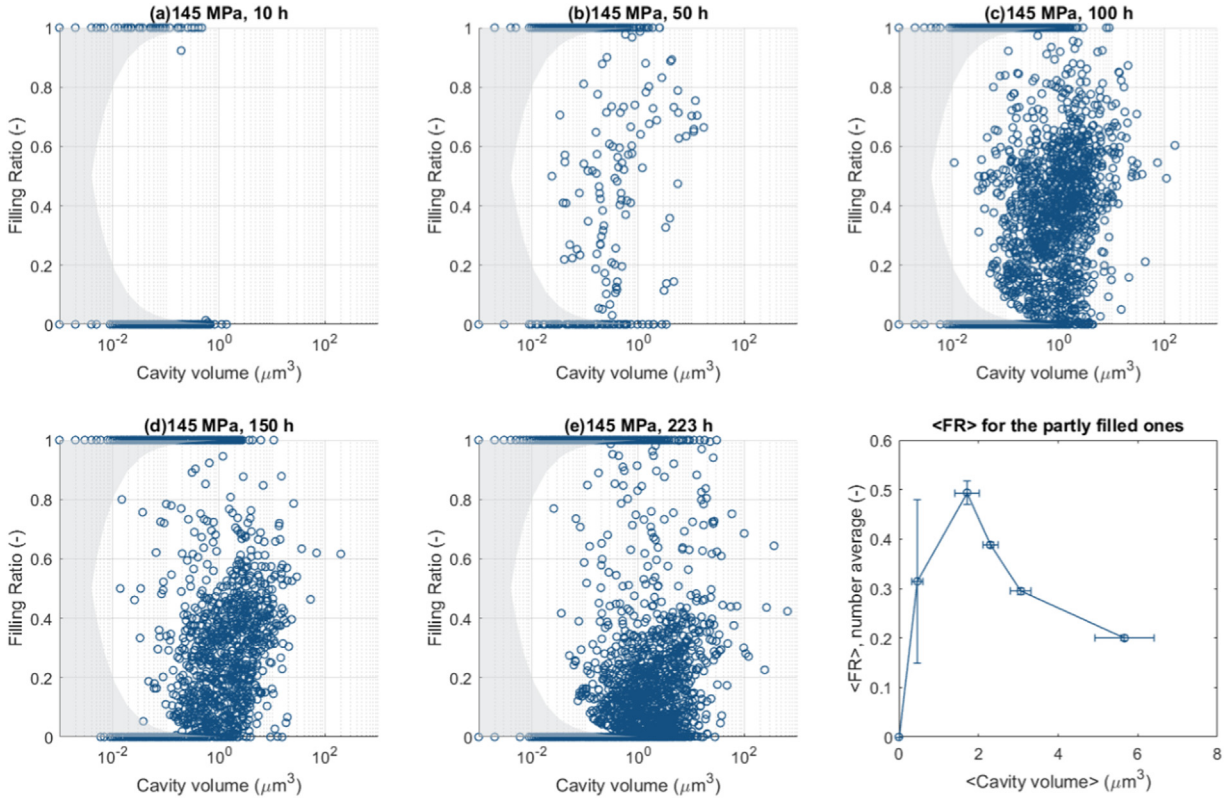

Fig. 7. (a–e) Filling ratio FR of individual cavities as a function of the cavity volume (sum of the open volume and the precipitation volume at the cavity surface) for the Fe-Au-W alloy after different creep times. (f) Average filling ratio ⟨FR⟩ as a function of the average cavity volume for the partly filled cavities. The grey shaded area indicates the resolution limit for the determination of the filling ration FR of the partially filled cavities.

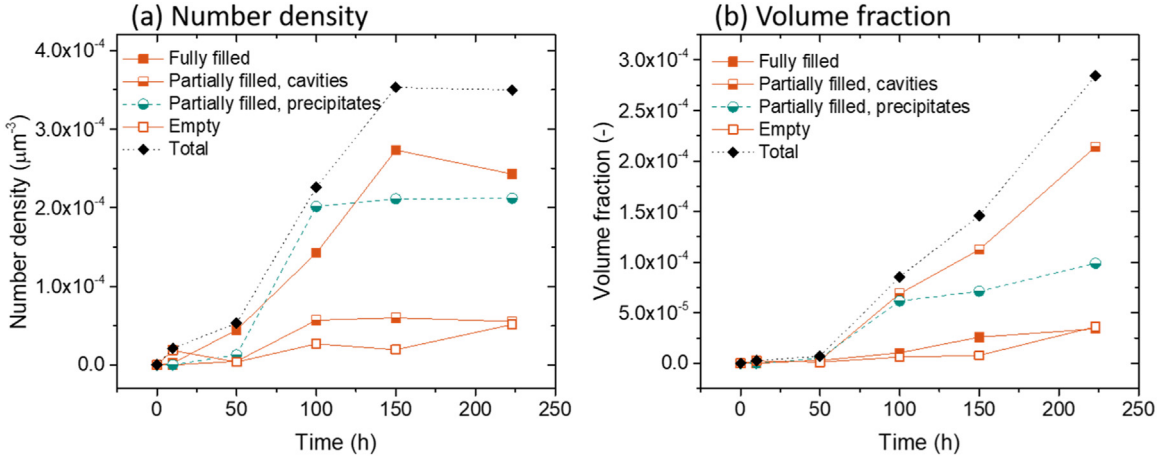

Fig. 8. Time evolution of (a) the number density and (b) the volume fraction of the cavities. Three groups of cavities (empty, partially-filled and fully-filled) are categorised based on their degree of filling. The data for the precipitates in the partially filled cavities are also presented for comparison.

tion. The fitting parameters for the ternary Fe-Au-W alloy are summarised in Table S1. The previously obtained fitting parameters of the Fe-Au [15] and Fe-W [21] binary alloys are also shown for comparison. Generally, the size of the cavities and precipitates in the Fe-Au-W ternary system is comparable with those of the Fe-Au binary system, but the number density and volume fraction for the two systems shows obvious differences, which are mainly caused by: (1) the difference in their experimental conditions (interrupted experiments for Fe-Au-W versus creep-failed experiments for Fe-Au) and (2) the limited linkage of the cavities observed for the Fe-Au-W alloy.

4.2. Nucleation of cavities and precipitates

During creep, the cavities preferentially nucleate at the grain boundaries, before they are being filled by the precipitates. The nucleation rate of the grain boundary cavities can be estimated by plotting the number of cavities per grain as a function of time, as shown in Fig. 10(a). Assuming that the volume illuminated by the synchrotron is made up of repetitive units with the size of d_g^3 (d_g being the grain size), and that each unit contains one transverse grain boundary that collects all the cavities and precipitates, then the number of cavities per grain can be estimated by $N_0 d_g^3$, where

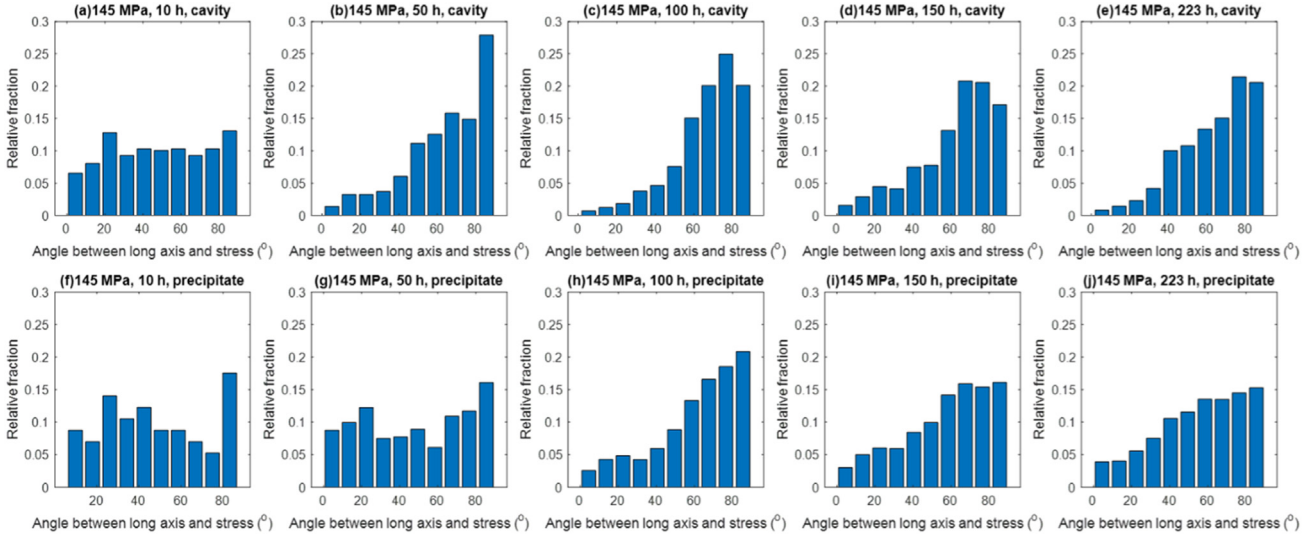

Fig. 9. Distribution of the angle between the long axis of the cavities ((a–e)) / precipitates ((f–j)) and the loading direction for different creep times. An angle of 90° indicates that the corresponding cavity / precipitate is oriented perpendicular to the load direction.

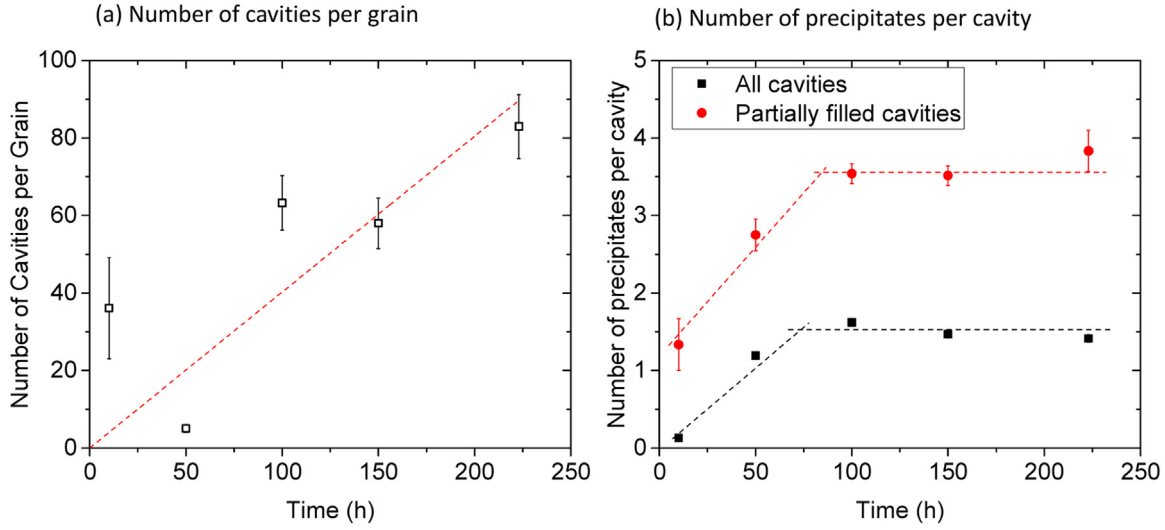

Fig. 10. (a) Number of cavities per grain as a function of the creep time. The data are fitted linearly with a straight line through the origin. (b) Number of precipitates per cavity as a function of time. The black data points are the average number of precipitate per cavity, while the red data points correspond to the average number of precipitates in partially-filled cavities. The dashed lines are a guide to the eye (For interpretation of the references to color in this figure legend, the reader is referred to the web version of this article.).

N_0 is the number density of cavities (listed in Table S1). In a study by Wu and co-workers [40] it was found that the number of cavities per unit area is proportional with the strain in low-alloyed steels. In the present work, where the strain rate is generally constant, we assume that the nucleation of cavities is continuous and that the number of cavities is proportional with the creep time. As the number of nucleated cavities is expected to be zero at the start of the creep test, a linear fit of the data in Fig. 10(a) yields a nucleation rate of 0.40(7) cavities/grain/h for the Fe-Au-W alloy (at 145 MPa and 550 °C). This value is lower than the result from the Fe-W alloy, which is 1.35(5) cavities/grain/h (at 140 MPa and 550 °C) [21]. However, given the difference in the grain size for the two systems with $d_g = 77$ µm for Fe-Au-W and $d_g = 127$ µm for Fe-W, the nucleation rate per unit grain-boundary area is comparable for the two alloys. For a grain-boundary area of $100 \times 100\ \mu m^2$ (oriented perpendicular to the stress) the estimated cavity nucleation rate is 0.67(12) cavity/h for the Fe-Au-W alloy and 0.84(3) cavity/h for the Fe-W alloy.

The average number of precipitates per cavity is shown in Fig. 10(b). Unlike the number of cavities per grain boundary, which keeps increasing with the creep time, the number of precipitates stabilises around 100 h to an average value of 1.5 precipitates per cavity. As this number is 0 for the empty cavities and 1 for the fully-filled cavities, this means that for the partially-filled cavities the number of precipitates per cavity needs to be larger than 1. As shown in Fig. 10(b), the number of precipitates per cavity for the partially-filled cavities is found to increase up to a creep time of 100 h and then stabilises at 3 to 4 precipitates per cavity, indicating a continuous nucleation of new precipitates at the cavity surface. This is consistent with the results shown Fig. 8(a).

It is worth to note that the average number of precipitates per cavity in the ternary Fe-Au-W alloy is approximately 3 times the value observed in the Fe-W binary alloy at a comparable stress level (145 MPa for Fe-Au-W and 140 MPa for Fe-W). Two reasons may be responsible for this. (1) Due to the limited diffusivity of W, the formation and growth of healing Laves phase in the Fe-

W system is slower than the Au-rich precipitates in the Fe-Au-W system. Therefore, more empty cavities exist in the Fe-W system, which results in a lower average number of precipitates per cavity. (2) Another reason is related to the limited size of the W-rich precipitates in the ternary system. From the 3D rendering shown in Fig. 6, the W-rich precipitates in the ternary alloy have a size of about 100 nm, and multiple W-rich precipitates are often found to contribute to the healing of a single cavity. In the Fe-W system [21], on the other hand, the W-rich precipitates range up to larger sizes, indicating that several precipitates can grow into a 'cluster' and thereby be analysed as a single healing precipitate within a cavity.

4.3. Growth of cavities and precipitates

In previous studies [15,21], the time evolution of cavity and precipitate was found to follow a power-law $V = kt^n$, where V is the average volume of the cavities (or precipitates) and t the creep time. The time exponent is 0.8 for the precipitates and the isolated cavities, while the linked cavities show a higher time exponent of 1.3 [15,21]. In Fig. 11(a,b) the average volume of the cavities and the precipitates in the ternary alloy is plotted as a function of creep time. For comparison, the time evolution for the volume of the cavities and precipitates in the binary systems is also presented. The blue and yellow regions correspond to the fitting results from the Fe-W system and Fe-Au system, respectively. The green areas represent the overlap of the two binary systems. The upper and lower limits represent the linked and isolated features, respectively. The average volume of the cavities in the ternary Fe-Au-W system lies in between that of the isolated cavities in the two binary systems, which is consistent with the observation that most cavities in the ternary Fe-Au-W system are isolated. The average volume for the precipitates in the ternary Fe-Au-W system shows a comparable behaviour as the precipitates in the binary Fe-Au alloy. The growth of both the cavities and the precipitates follows a power law $V = kt^n$. For the cavities, the time exponent n is 0.87(7), indicating a similar growth mechanism as the binary counterparts. The time exponent n for the precipitates yields 0.4(1) for the average volume of the individual precipitates. Considering the fact that potentially multiple precipitates are located in one cavity (as discussed in Section 4.2), the average value for the total precipitate volume within one cavity can also be calculated (red data points in Fig. 11(b)), which gives a fitted time exponent n of 0.6(1). These results indicate that the growth behaviour of the precipitates in the ternary system is similar to the binary systems when the precipitates within one cavity are treated as a whole.

Multiple dominating mechanisms have been proposed to describe the growth of creep cavities, including diffusion, plasticity, grain boundary sliding, or a combination of them [6]. In a coupled model [41–44], it is suggested that the creep cavities, being controlled by grain-boundary diffusion, are embedded in the power-law controlled deforming matrix. Generally, diffusional growth is dominant for smaller cavities, lower stress levels and lower temperatures, while plasticity dominates otherwise. A diffusion length $\Lambda = \left(\frac{D_{gb}\Omega\delta\sigma_0}{k_B T\dot{\varepsilon}}\right)^{1/3}$ [45] has been introduced, where D_{gb} is the diffusivity of vacancies at the grain boundary, δ the grain boundary thickness, Ω the atomic volume, σ_0 the applied stress, $\dot{\varepsilon}$ the strain rate, k_B the Boltzmann constant and T the temperature. The ratio between the cavity radius a and the diffusion length Λ can be used to estimate whether diffusional growth is dominant. As (a/Λ) increases, the creep flow becomes more important, and the power-law limit is reached when $(a/\Lambda) \to \infty$. In the ternary system, the diffusion length at a stress of 145 MPa and a temperature of 550 °C corresponds to $\Lambda \approx 30$ µm, which is larger than the average inter-cavity spacing (ranging from 4 to 7 µm for different creep times).

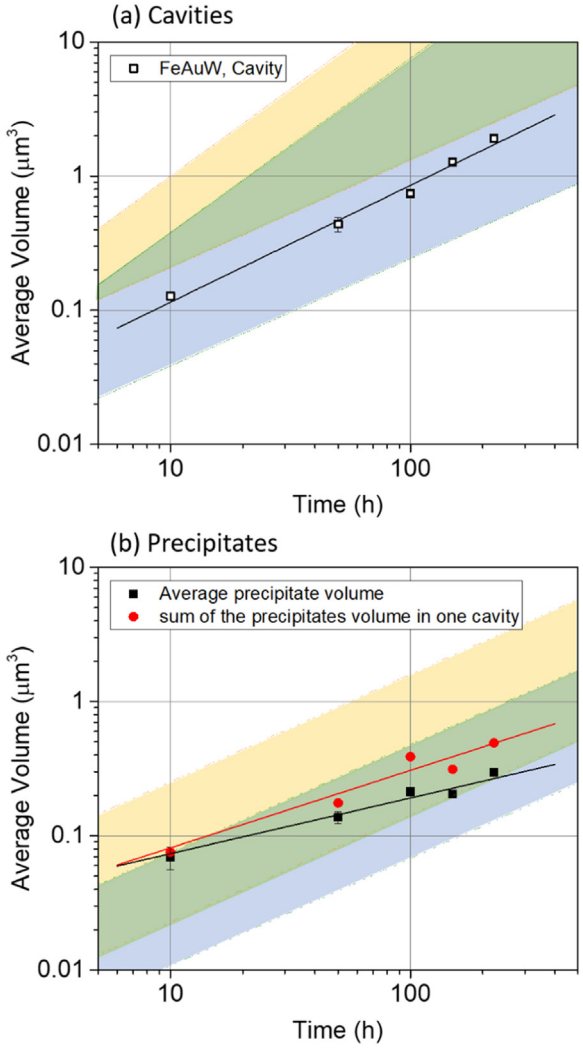

Fig. 11. Average volume $\langle V \rangle$ of (a) the cavities and (b) the precipitates as a function of time. The lines are fits to $\langle V \rangle = k\, t^{\,n}$. The blue and yellow shaded areas show the range of Fe-W and Fe-Au alloys, respectively and the green areas for the overlap. The upper and lower limits represent the linked and isolated features, respectively. In (b), the black data points are the average volumes of all the precipitates, while the red ones show the average value for the summed volume of the precipitates in each cavity. The fitting parameters are listed in Table S2 (supplementary information) (For interpretation of the references to color in this figure legend, the reader is referred to the web version of this article.).

It can therefore be assumed that the cavity growth in the Fe-Au-W ternary system is controlled by the vacancy diffusion through the grain boundaries, with an inward flux of $J_v = -\frac{1}{\Omega}\frac{D_{gb}x_v}{k_B T}\nabla\mu$, where x_v is the vacancy concentration at the grain boundary and $\nabla\mu$ the gradient in chemical potential, which is related to the stress gradient. Assuming that the stress distribution around one cavity does not change over time, the inward vacancy flux is then constant in time and the cavity volume increases linearly with time. This is consistent with the fitted time exponent n of 0.87(7) in Fig. 11(a).

Once a cavity is formed at the grain boundary, the autonomous healing starts to take place by depleting the supersaturated solute agents dissolved in the matrix. The solute in the vicinity of the grain boundary cavities depletes first, and the depletion zone then expands over time. Depending on (1) the ratio of the solute diffusivity in the grain boundary and in the bulk, and (2) the ratio between the inter-cavity spacing and the cavity diameter, the amount of solute atoms transported to a cavity scales as $V \propto t^n$, where the time exponent n ranges from 0.5 to 1 [24]. A time exponent of 0.6,

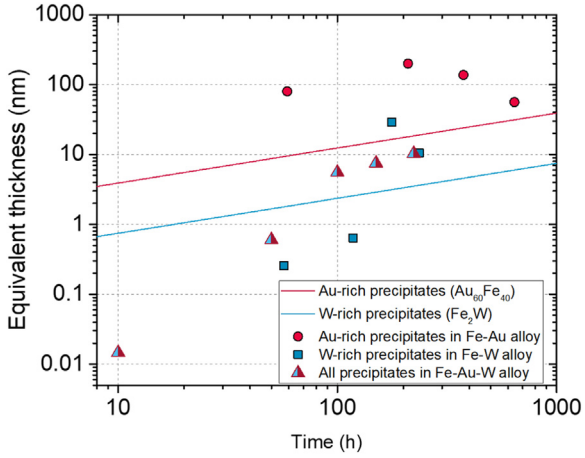

Fig. 12. Equivalent thickness l of the precipitation layer if all the precipitates were spread over the surface uniformly. The solid lines are calculated assuming 1D diffusion by $l(t) = (4/\sqrt{\pi})(\Delta x/x_p)\sqrt{D_x t}$, where Δx is the supersaturated solute fraction, x_p the solute fraction in the precipitate and D_X the solute (volume) diffusivity of element X. The experimental data are calculated by $f_V d_g$, where f_V and d_g are the volume fraction of the precipitates and the grain size, respectively.

as shown in Fig. 11(b), indicates a cross-over from 2D to 1D diffusion (see the fitting parameters listed in Table S2).

In the Fe-Au-W alloy, the solute diffusivity in the grain boundary is much higher (about a factor 10^6) than that in the bulk. For a ratio between the inter-cavity spacing λ and the cavity diameter a of $\lambda/a < 20$, a 1D diffusion profile is expected to develop over time [24]. In this situation, the total amount of the solute agents transported to the grain-boundary creep cavities scales with the 1D matrix diffusion length towards the grain boundary $2\sqrt{D_m t}$, where D_m is the solute diffusivity in the matrix and t the creep time. To monitor the total amount of solute involved in the cavity filling, we calculated the equivalent precipitates layer thickness (i.e., the equivalent thickness of the precipitation layer on the surface if the precipitates are spread out over the grain boundary, covering it uniformly). The experimentally derived equivalent precipitates layer thickness for the ternary Fe-Au-W alloy is shown in Fig. 12. The values for the binary Fe-Au and Fe-W alloys are also presented for comparison. In addition to the experimental data points the predictions for 1D diffusion of supersaturated Au and W are indicated by solid lines.

The experimental data points for Fe-Au-W alloy clearly demonstrate the development of the 1D diffusion after a creep time of about 100 h, as the time evolution of the equivalent layer thickness closely follows the $t^{1/2}$ power law predicted for 1D diffusion (for shorter times a faster growth rate is found). The experimental equivalent thickness for the ternary alloy is less than the calculated thickness for Au-rich precipitates. This indicates that the 1D solute diffusion is constrained by the availability of free cavity surface in partially filled cavities. The calculated layer thickness can therefore only act as an upper bound. The solute diffusion in the binary Fe-Au and Fe-W alloys, however, seems to be enhanced to a certain extent. In Fe-Au system [18] a higher effective diffusivity (two orders magnitude higher than the bulk diffusivity) was observed, resulting from an enhanced sub-grain formation during creep. For the Fe-W system, the enhancement in solute diffusivity may have resulted from the relatively large creep strain and the higher strain rate, compared to the Au-containing alloys. A higher creep rate is accompanied with the generation of excess vacancies [46,47], which accelerate the diffusivity of both the solute and the host atoms. Militzer and co-workers [46] have proposed that during high-temperature deformation, the excess vacancy concentration first increases with time, then it drops and approaches the steady-state value due to the vacancy annihilation at grain boundaries and dislocations. The strain rate in the Fe-W alloy (about 10^{-4} h^{-1} at 550 °C) yields an excess vacancy concentration that is about 30 times higher than the thermal equilibrium value, which can result in an enhanced diffusivity.

It is interesting to note that W-rich precipitates seem to have a very limited contribution in the cavity healing in the Fe-Au-W alloy. In fact, in the ROI as shown in Fig. 6, W-rich precipitates have taken only about 5% of the total volume of all the precipitates. While in Fig. 12, it is indicated that at the same creep time, the W-rich precipitation is expected to be at a level of 20% compared to the Au-rich precipitation. It is, however, not yet determined that tungsten diffusion is constrained in the Fe-Au-W alloy. In a previous study on free surface precipitation for the Fe-Au-W, Fe-Au and Fe-W alloys [39], the nucleation of W-rich precipitates in the Fe-Au-W ternary alloy also showed some delay. At a temperature of 700 °C a large amount of W-rich precipitates was formed at the outer free surface of the Fe-Au-W alloy sample. The overall surface precipitation kinetics at the outer sample surface of the Fe-Au-W alloy was not significantly suppressed compared to that of the Fe-W alloy. Since the creep experiments in the present study were performed at a lower temperature, longer creep times may be necessary for a more complete investigation on the effectiveness of the W-rich precipitation kinetics to achieve self healing of creep damage.

4.4. Healing mechanism

In previous synchrotron X-ray tomography studies [15,21], it was found that the isolated and linked cavities show a different healing behaviour. The isolated cavities can be healed continuously until a fully filling is achieved, while a linkage of the cavities can cause a sharp drop in filling ratio. In the present work, linkage of the cavities is rare due to the limited creep strain, as discussed in Section 3.4. Nevertheless, as shown in Fig. 7, the average filling ratio of the partly filled cavities decreases with time, and the majority of the data points shifts towards the right bottom, indicating an increasing cavity volume and a decreasing average filling ratio. As shown in Fig. 12, the solute diffusion generally follows a 1D character after a creep time of 100 h, which results in a decreasing solute flux towards the grain boundary. This indicates that if a cavity is formed at a later creep stage, when the solute flux from the matrix to the creep cavity is reduced by the development of the 1D diffusion profile, more time will be needed to fully fill the cavity. Another reason for the decreasing filling ratio is the continuous nucleation of cavities, and therefore the decrease in the average inter-cavity spacing. In the work by Versteylen and co-workers [24], it is demonstrated that within the 1D diffusion regime, the time to full filling scales with $(\lambda/d_{cav})^4$, where λ is the inter-cavity spacing and d_{cav} is the diameter of the cavity. For a grain boundary with a constant nucleation rate per unit of surface area $\dot{N}$, the inter-cavity spacing corresponds to $\lambda = (\dot{N}t)^{-1/2}$, where t is the creep time. The time evolution of the cavity diameter scales as $d \propto V^{1/3} \propto t^{0.3}$, where cavity volume scales as $V \propto t^{0.87}$, as discussed in Section 4.3. The ratio between the inter-cavity spacing and the cavity diameter then scales as $(\lambda/d_{cav}) \propto t^{-0.8}$, which agrees well with the experimental observation of $(\lambda/d_{cav}) \propto t^{-0.6(1)}$ in Fig. S5 (Supplementary Information). Therefore, the time required to fully fill a cavity of a fixed size increases significantly for longer nucleation times. Assuming a cavity nucleated at the grain boundary, and it starts to be healed at $t = t_0$ (t_0 is after the nucleation time). The cavity volume yields

$$V_{cav} = V_0 + k(t - t_0)^n \quad (2)$$

where k and n are fitting parameters for cavity growth, and V_0 the volume of the cavity when its healing starts.

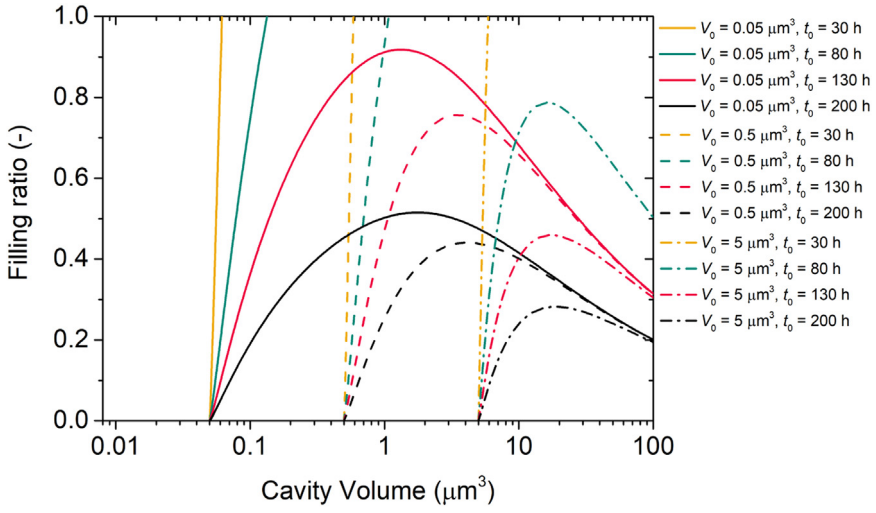

Fig. 13. Prediction of the filling ratio of the cavities with a different time t_0 (indicated by different colours) and a different volume V_0 (indicated by different line types), where V_0 is the volume of the cavity when its healing starts, and t_0 the time when healing starts. The nucleation rate of the cavities is fixed at 0.4/grain/h.

The precipitates form due to solute atoms diffusing towards the cavity surface from both sides of the grain boundary, and this process can be simplified to a 1D diffusion problem. The solute atoms first diffuse towards the nearest grain boundaries from both sides, and then migrate through the grain boundary (acting as a fast diffusion path), before being transferred to the cavity surface. From t_0 to t, the sum volume of the healing agent (and therefore the precipitate volume) corresponds to

$$V_{ppt} = 2\lambda^2 \frac{\Delta x}{x_p} \frac{1}{\sqrt{\pi}} \left(2\sqrt{D_X t} - 2\sqrt{D_X t_0}\right) \tag{3}$$

where $\Delta x = x_\infty - x_e$ is the supersaturation of the solute, x_p the concentration of the solute element in the precipitate phase, D_X the diffusivity of solute X, λ the inter-cavity spacing. $2\sqrt{D_X t}$ and $2\sqrt{D_X t_0}$ correspond to the solute diffusion length at t and t_0, respectively. A schematic representation is given in Fig. S6(a) (supplementary information). When healing starts at time t_0, the inter-cavity spacing is

$$\lambda = \frac{d_g}{\sqrt{\dot{N}_g t_0}} \tag{4}$$

where d_g is the grain size, $\dot{N}_g$ the nucleation rate (per grain per unit of time). Therefore, Eq. (3) can be written as

$$V_{ppt} = 4\frac{d_g^2}{\dot{N}_g t_0} \frac{\Delta x}{x_p} \frac{\sqrt{D_X}}{\sqrt{\pi}} \left(\sqrt{t} - \sqrt{t_0}\right) \tag{5}$$

The filling ratio of the cavity can then be calculated by V_{ppt}/V_{cav}. Taking $\dot{N}_g$ = 0.4/grain/h (as discussed in Section 4.2), $D_{Au} = 7.4 \times 10^{-19}$ m^{2}s^{-1} at 550 °C [25] (since Au is the dominating healing agent), $x_p = 0.6$, $\Delta x = 0.01$ and $d_g = 77$ μm, For cavities with different starting volumes and different start-healing times, the filling ratios versus cavity volume are shown in Fig. 13. It is clear that for a cavity that nucleated later (and therefore its healing also starts later), more time is required to achieve a fully filling. For the cavities nucleated at late stage of creep, their filling ratios eventually show an upper limit, after which the filling ratio decreases with time. This behaviour qualitatively agrees with the time evolution of the filling ratios presented in Fig. 7. For each V_0, a critical time can be derived, and if a cavity starts to be filled after this time, it is less likely to be fully filled. It is worth to note that a higher cavity nucleation rate (which can be resulted from a higher stress level) leads to a faster decrease in the inter-cavity spacing, and therefore a lower overall filling ratio, as shown in Fig. S6(b) (Supplementary information).

5. Conclusion

Creep experiments with a constant applied stress of 145 MPa at a temperature of 550 °C were performed on a high-purity ternary Fe-Au-W alloy with 1 at.% supersaturation for both Au and W at the creep temperature to study the autonomous healing of grain-boundary cavities by Au-rich and W-rich precipitates. The development of the creep cavities and the healing precipitates at different creep stages was investigated by performing synchrotron X-ray nano-tomography on different samples being exposed to the same creep condition for different loading times.

The main conclusions are:

(1) During creep, the grain-boundary cavities are continuously formed and subsequently healed by precipitation on the cavity surface. The sequential order is proven by: (a) the similarity in morphology of cavities and precipitates, (b) the development of the angle between the long-axis and the load direction for cavities and precipitates and (c) the time evolution of the distribution of the empty, partially-filled and fully-filled cavities.

(2) Compared to the binary Fe-Au and Fe-W counterparts, the linkage of the cavities in the ternary Fe-Au-W system is rare, due to the limited creep strain and the low strain rate. The cavities in the ternary system show similar nucleation and growth behaviour as the cavities in the Fe-W alloy. In the Fe-Au-W alloy the solute diffusion is not significantly enhanced by a relatively high sub-grain formation (Fe-Au alloy) or a relatively high strain rate (Fe-W alloy).

(3) Cavities nucleated at an early creep stage can be fully healed, while due to a decrease in the diffusional solute flux and the inter-cavity spacing over time, a longer time is required to fully fill the late formed cavities. This results in an overall decrease in filling ratio of the partially filled but still growing cavities with time.

(4) High-resolution tomography with a resolution of 30 nm allows for a 3D segmentation of the Au-rich and the relatively small W-rich precipitates (about 100 nm in size). The results are in accordance with the 2D observation from SEM and TEM images. However, for the situation where Au-rich and W-rich precipitates form in contact to each other, an even higher resolution is sometimes required for proper segmentation due to the

small size of W-rich precipitates and the limited contrast between both precipitates.

(5) The supersaturated Au solute diffuses significantly faster than the supersaturated W. This results in a fast filling of creep cavities by Au-rich precipitates and a relatively slow filling by W-rich precipitates. This difference in healing kinetics indicates that supersaturated Au and W provide two healing agents that operate on different time scales. Combining both can significantly extend the time scale over which self healing of creep damage can potentially be achieved.

Declaration of Competing Interest

The authors declare that they have no known competing financial interests or personal relationships that could have appeared to influence the work reported in this paper.

Acknowledgements

We thank C. Kwakernaak for providing the SEM facilities. We acknowledge D. Ngan-Tillard and Y. Li for technical assistance with the data analysis. The X-ray synchrotron nanotomography experiments were performed on beamline ID16A-NI at the European Synchrotron Radiation Facility (ESRF), Grenoble, France. We are grateful to the beamline staff at the ESRF for providing assistance in using beamline ID16A-NI. Y. Fu acknowledges the financial support provided by the China Scholarship Council (CSC).

Supplementary materials

Supplementary material associated with this article can be found, in the online version, at doi:10.1016/j.actamat.2022.118266.

References

[1] J.N. Greenwood, D.R. Miller, J.W. Suiter, Intergranular cavitation in stressed metals, Acta Metall. Mater. 2 (2) (1954) 250–258.
[2] F.R.N. Nabarro, H.L. de Villiers, The Physics of Creep: Creep and Creep-Resistant Alloys, 1st ed., CRC Press, 1995.
[3] M. Taneike, F. Abe, K. Sawada, Creep-strengthening of steel at high temperatures using nano-sized carbonitride dispersions, Nature 424 (6946) (2003) 294–296.
[4] F. Abe, Progress in creep-resistant steels for high efficiency coal-fired power plants, J. Press. Vessel Technol. 138 (4) (2016) 040804.
[5] F. Abe, A. Shirzadi, S. Jackson, Development of creep-resistant steels and alloys for use in power plants, in: Structural Alloys for Power Plants, Woodhead Publishing, 2014, pp. 250–293.
[6] M.E. Kassner, T.A. Hayes, Creep cavitation in metals, Int. J. Plast. 19 (10) (2003) 1715–1748.
[7] M.D. Hager, P. Greil, C. Leyens, S. van der Zwaag, U.S. Schubert, Self-healing materials, Adv. Mater. 22 (47) (2010) 5424–5430.
[8] N. van Dijk, S. van der Zwaag, Self-healing phenomena in metals, Adv. Mater. Interfaces 5 (17) (2018) 1800226.
[9] B. Grabowski, C.C. Tasan, M.D. Hager, S. van der Zwaag, U.S. Schubert, Self-Healing Metals, in: Self-Healing Materials, Springer International Publishing, Cham, Switzerland, 2016, pp. 387–407.
[10] K. Laha, J. Kyono, S. Kishimoto, N. Shinya, Beneficial effect of B segregation on creep cavitation in a type 347 austenitic stainless steel, Scr. Mater. 52 (7) (2005) 675–678.
[11] K. Laha, J. Kyono, T. Sasaki, S. Kishimoto, N. Shinya, Improved creep strength and creep ductility of type 347 austenitic stainless steel through the self-healing effect of boron for creep cavitation, Metall. Mater. Trans. A 36 (2) (2005) 399–409.
[12] S.M. He, P.N. Brandhoff, H. Schut, S. van der Zwaag, N.H. van Dijk, Positron annihilation study on repeated deformation/precipitation aging in Fe–Cu–B–N alloys, J. Mater. Sci. 48 (18) (2013) 6150–6156.
[13] S.M. He, N.H. van Dijk, M. Paladugu, H. Schut, J. Kohlbrecher, F.D. Tichelaar, S. van der Zwaag, *In-situ* determination of aging precipitation in deformed Fe-Cu and Fe-Cu-B-N alloys by time-resolved small-angle neutron scattering, Phys. Rev. B 82 (17) (2010) 174111.
[14] S.M. He, N.H. van Dijk, H. Schut, E.R. Peekstok, S. van der Zwaag, Thermally activated precipitation at deformation-induced defects in Fe-Cu and Fe-Cu-B-N alloys studied by positron annihilation spectroscopy, Phys. Rev. B 81 (9) (2010) 094103.
[15] H. Fang, C.D. Versteylen, S. Zhang, Y. Yang, P. Cloetens, D. Ngan-Tillard, E. Brück, S. van der Zwaag, N.H. van Dijk, Autonomous filling of creep cavities in Fe-Au alloys studied by synchrotron X-ray nano-tomography, Acta Mater. 121 (2016) 352–364.
[16] S. Zhang, J. Kohlbrecher, F.D. Tichelaar, G. Langelaan, E. Brück, S. van der Zwaag, N.H. van Dijk, Defect-induced Au precipitation in Fe–Au and Fe–Au–B–N alloys studied by in situ small-angle neutron scattering, Acta Mater. 61 (18) (2013) 7009–7019.
[17] S. Zhang, C. Kwakernaak, W. Sloof, E. Brück, S. van der Zwaag, N. van Dijk, Self healing of creep damage by gold precipitation in iron alloys, Adv. Eng. Mater. 17 (5) (2015) 598–603.
[18] S. Zhang, C. Kwakernaak, F.D. Tichelaar, W.G. Sloof, M. Kuzmina, M. Herbig, D. Raabe, E. Brück, S. van der Zwaag, N.H. van Dijk, Autonomous repair mechanism of creep damage in Fe-Au and Fe-Au-B-N alloys, Metall. Mater. Trans. A 46 (12) (2015) 5656–5670.
[19] S. Zhang, G. Langelaan, J.C. Brouwer, W.G. Sloof, E. Brück, S. van der Zwaag, N.H. van Dijk, Preferential Au precipitation at deformation-induced defects in Fe–Au and Fe–Au–B–N alloys, J. Alloy. Compd. 584 (2014) 425–429.
[20] S. Zhang, H. Fang, M.E. Gramsma, C. Kwakernaak, W.G. Sloof, F.D. Tichelaar, M. Kuzmina, M. Herbig, D. Raabe, E. Brück, S. van der Zwaag, N.H. van Dijk, Autonomous filling of grain-boundary cavities during creep loading in Fe-Mo alloys, Metall. Mater. Trans. A 47 (10) (2016) 4831–4844.
[21] H. Fang, N. Szymanski, C.D. Versteylen, P. Cloetens, C. Kwakernaak, W.G. Sloof, F.D. Tichelaar, S. Balachandran, M. Herbig, E. Brück, S. van der Zwaag, N.H. van Dijk, Self healing of creep damage in iron-based alloys by supersaturated tungsten, Acta Mater 166 (2019) 531–542.
[22] Y. Fu, C. Kwakernaak, W.G. Sloof, F.D. Tichelaar, E. Brück, S. van der Zwaag, N.H. van Dijk, Competitive healing of creep-induced damage in a ternary Fe-3Au-4 W alloy, Metall. Mater. Trans. A 51 (9) (2020) 4442–4455.
[23] C.D. Versteylen, M.H.F. Sluiter, N.H. van Dijk, Modelling the formation and self-healing of creep damage in iron-based alloys, J. Mater. Sci. 53 (20) (2018) 14758–14773.
[24] C.D. Versteylen, N.K. Szymański, M.H.F. Sluiter, N.H. van Dijk, Finite element modelling of creep cavity filling by solute diffusion, Philos. Mag. 98 (10) (2018) 864–877.
[25] C.D. Versteylen, N.H. van Dijk, M.H.F. Sluiter, First-principles analysis of solute diffusion in dilute bcc Fe-X alloys, Phys. Rev. B 96 (9) (2017) 094105.
[26] H. Yu, W. Xu, S. van der Zwaag, A first step towards computational design of W-containing self-healing ferritic creep resistant steels, Sci. Technol. Adv. Mater. 21 (1) (2020) 641–652.
[27] A. Isaac, F. Sket, W. Reimers, B. Camin, G. Sauthoff, A.R. Pyzalla, In situ 3D quantification of the evolution of creep cavity size, shape, and spatial orientation using synchrotron X-ray tomography, Mater. Sci. Eng. A 478 (1–2) (2008) 108–118.
[28] A. Pyzalla, B. Camin, T. Buslaps, M. Di Michiel, H. Kaminski, A. Kottar, A. Pernack, W. Reimers, Simultaneous tomography and diffraction analysis of creep damage, Science 308 (5718) (2005) 92–95.
[29] R. Kumar, J. Villanova, P. Lhuissier, L. Salvo, *In situ* nanotomography study of creep cavities in Al-3.6-Cu alloy, Acta Mater. 166 (2019) 18–27.
[30] M. Huppmann, B. Camin, A.R. Pyzalla, W. Reimers, In-situ observation of creep damage evolution in Al-Al_2O_3 MMCs by synchrotron X-ray microtomography, Int. J. Mater. Res. 101 (3) (2010) 372–379.
[31] P. Cloetens, W. Ludwig, J. Baruchel, D. Van Dyck, J. Van Landuyt, J.P. Guigay, M. Schlenker, Holotomography: quantitative phase tomography with micrometer resolution using hard synchrotron radiation x rays, Appl. Phys. Lett. 75 (19) (1999) 2912–2914.
[32] G. Ghosh, G.B. Olson, The isotropic shear modulus of multicomponent Fe-base solid solutions, Acta Mater. 50 (10) (2002) 2655–2675.
[33] H.J. Frost, M.F. Ashby, R.I. Jaffee, B.A. Wilcox, Deformation-mechanism maps for pure iron, two austenitic stainless steels, and a low-alloy ferritic steel, in: Fundamental Aspects of Structural Alloy Design, Springer US, Boston, MA, 1977, pp. 27–65.
[34] O.D. Sherby, Factors affecting the high temperature strength of polcyrystalline solids, Acta Metall. Mater. 10 (2) (1962) 135–147.
[35] A. Somogyi, B. Lai, P. Cloetens, S. Bohic, M. Salome, L. Bloch, M. Hubert, F. Fus, Y. Yang, A. Pacureanu, J.C. da Silva, High-energy cryo x-ray nano-imaging at the ID16A beamline of ESRF, in: Proceedings of the X-Ray Nanoimaging: Instruments and Methods III, 2017.
[36] A. Mirone, E. Brun, E. Gouillart, P. Tafforeau, J. Kieffer, The PyHST2 hybrid distributed code for high speed tomographic reconstruction with iterative reconstruction and a priori knowledge capabilities, Nucl. Instrum. Methods B 324 (2014) 41–48.
[37] DIPimage (2019), MATLAB toolbox, Quantitative Imaging Group, Delft University of Technology, the Netherlands. Retrieved from https://diplib.org/.
[38] K. Maruyama, F. Abe, T.U. Kern, R. Viswanathan, 8 - fundamental aspects of creep deformation and deformation mechanism map, in: Creep-Resistant Steels, Woodhead Publishing, 2008, pp. 265–278.
[39] Y. Fu, C. Kwakernaak, J.C. Brouwer, W.G. Sloof, E. Brück, S. van der Zwaag, N.H. van Dijk, Surface precipitation of supersaturated solutes in a ternary Fe–Au–W alloy and its binary counterparts, J. Mater. Sci. 56 (8) (2020) 5173–5189.
[40] R. Wu, R. Sandström, Strain dependence of creep cavity nucleation in low alloy and 12%Cr steels, Mater. Sci. Technol. 12 (5) (1996) 405–415.
[41] W. Beere, M.V. Speight, Creep cavitation by vacancy diffusion in plastically deforming solid, Met. Sci. J. 12 (4) (1978) 172–176.

[42] G.H. Edward, M.F. Ashby, Intergranular fracture during power-law creep, Acta Metall. Mater. 27 (9) (1979) 1505–1518.
[43] A. Needleman, J.R. Rice, Plastic creep flow effects in the diffusive cavitation of grain-boundaries, Acta Metall. Mater. 28 (10) (1980) 1315–1332.
[44] E. Van Der Giessen, M.W.D. Van Der Burg, A. Needleman, V. Tvergaard, Void growth due to creep and grain boundary diffusion at high triaxialities, J. Mech. Phys. Solids 43 (1) (1995) 123–165.
[45] I.W. Chen, A.S. Argon, Diffusive growth of grain-boundary cavities, Acta Metall. Mater. 29 (10) (1981) 1759–1768.
[46] M. Militzer, W.P. Sun, J.J. Jonas, Modelling the effect of deformation-induced vacancies on segregation and precipitation, Acta Metall. Mater. 42 (1) (1994) 133–141.
[47] S.H. Song, X.M. Chen, L.Q. Weng, Solute diffusion during high-temperature plastic deformation in alloys, Mater. Sci. Eng. A 528 (24) (2011) 7196–7199.